CrystEngComm

ROYAL SOCIETY OF CHEMISTRY

PAPER

View Article Online
View Journal | View Issue

Cite this: *CrystEngComm*, 2025, **27**, 146

Elastic, dielectric and piezoelectric properties of a $EuCa_4O(BO_3)_3$ high-temperature piezoelectric crystal

Jie Feng, Linwen Jiang, Zhigang Sun, Chen Yang and Yanqing Zheng *

Received 1st September 2024,
Accepted 11th November 2024

DOI: 10.1039/d4ce00876f

rsc.li/crystengcomm

The rare-earth oxyborate crystal $RCa_4O(BO_3)_3$ (RCOB, R: rare-earth elements) is an inorganic photoelectric multifunctional material, which has important applications in the field of high-temperature piezoelectricity. In this work, a $EuCa_4O(BO_3)_3$ (EuCOB) crystal with a diameter of 25 mm was successfully grown by the Bridgman method. The thermal conductivity, thermal diffusivity and specific heat of the EuCOB crystal at high temperature were measured. The dielectric coefficient, electromechanical coupling coefficient, elastic coefficient and piezoelectric coefficient of the EuCOB crystal at high temperature were measured by the resonance–antiresonance method. In particular, the shear piezoelectric coefficient d_{26} of the EuCOB crystal is 7.01 pC N^{-1} at room temperature and 6.22 pC N^{-1} at 800 °C, with a small variation of 11.4%. The electrical resistivities of the EuCOB crystal along the *X*, *Y* and *Z* directions at 800 °C are 5.8×10^7 Ω cm, 3.1×10^7 Ω cm and 2.9×10^7 Ω cm, respectively. The large piezoelectric coefficient and high electrical resistivity indicate the potential application of the EuCOB crystal in a high-temperature piezoelectric field.

1. Introduction

In recent years, high-temperature piezoelectric sensors have attracted more and more attention. They play an important role in aerospace, automobile manufacturing, energy and other fields. For example, the vibration detection of key components such as aircraft and automobile engines is carried out under a high-temperature work environment that requires the accuracy and stability of high-temperature piezoelectric sensors.[1–4] Therefore, high-temperature piezoelectric sensors usually require a high resistivity, low dielectric loss, good temperature stability of electromechanical performance, and high piezoelectric coefficient.[5–7] The core component is a high-temperature piezoelectric crystal. Traditional high-temperature piezoelectric crystals include quartz, lithium niobate, langasite-type crystal, *etc.* Quartz has the advantages of a high electrical resistivity and low-temperature coefficient. However, its low electromechanical coefficient, low piezoelectric coefficient, high loss above 350 °C, and α–β phase transition at about 573 °C limit its application in a high-temperature piezoelectric field.[8–10] Lithium niobate has a high electromechanical coefficient, but its resistivity is low. It is easy to be decomposed at high temperature, and the work temperature is limited to 600 °C.[11,12] The langasite-type crystal is considered to be one of the promising candidate crystals for high-temperature sensors. There is no phase transition before its melting point (1320–1470 °C).[13,14] However, it has a relatively low resistivity and low quality factor at high temperature.[15–18] High-temperature crystals with high resistivity and high piezoelectric coefficients are the goals pursued in the field of high-temperature piezoelectricity. So far, most of these piezoelectric crystals have their own limitations in practical high-temperature applications, which cannot meet the demands of high-temperature piezoelectric sensors. Therefore, there is an urgent need to develop high-temperature piezoelectric crystals with both high piezoelectric coefficient and high electrical resistivity.

New high-temperature piezoelectric crystals $RCa_4O(BO_3)_3$ (RCOB, R: rare-earth elements) have become one of the important directions in the research and application of high-temperature piezoelectric materials due to their excellent thermal stability and piezoelectric properties.[19–26] The RCOB crystal belongs to the monoclinic system, m point group, and C_m space group. RCOB crystals can be grown by replacing the R^{3+} ions that occupy the distorted R(1)–O octahedron, and different RCOB crystals have different properties.[27] In the report, the RCOB crystal has extremely high electrical resistivity, strong electromechanical performance, stable electromechanical performance at high temperature, stable chemical properties at high temperature, and no phase transition before the melting point (1420–1510 °C).[28–31] The electrical resistivity of the RCOB crystal at high temperatures (10^6–10^8 Ω cm) is 1–2 orders of magnitude higher than that of the CTGS crystal, and the effective piezoelectric coefficient (7.6–16.5 pC N^{-1}) is more than three times higher than that

School of Materials Science and Chemical Engineering, Ningbo University, Ningbo, Zhejiang 315211, P. R. China. E-mail: zhengyanqing@nbu.edu.cn

of the quartz crystal, showing the application advantages of high-temperature piezoelectric sensors.[32–37] Among all the feasible RCOB crystals, the EuCOB crystal has not been fully studied, including its dielectric constant, elastic constant, piezoelectric constant, electrical resistivity and temperature dependence.

Therefore, this work attempts to design, grow and characterize a EuCOB crystal. A EuCOB single crystal with a diameter of 25 mm was successfully grown by the Bridgman method. The piezoelectric coefficient, dielectric coefficient, elastic coefficient and electrical resistivity of the EuCOB crystal at high temperature were reported for the first time, and its thermal properties were characterized and analyzed for exploring its potential in high-temperature piezoelectric applications.

2. Experimental section

2.1 Polycrystalline synthesis

Pure phase EuCOB polycrystalline powders were synthesized by a high-temperature solid-phase method. The chemical reaction equation is as follows:

$$Eu_2O_3 + 8CaCO_3 + 6H_3BO_3 = 2EuCa_4O(BO_3)_3 + 8CO_2\uparrow + 9H_2O\uparrow$$

High purity Eu_2O_3 (4N), $CaCO_3$ (4N) and H_3BO_3 (4N) were stoichiometrically weighed. In addition, excessive boric acid (3%) was added to avoid the influence of volatility on the crystal quality. The powders were compressed under a pressure of 300 MPa into a cylindrical block with a diameter of 60 mm and sintered at 1100 °C for 10 hours. After the first sintering, the product was smashed, ground into powders, remixed, and then pressed into a cylindrical block with a diameter of 60 mm. Finally, the cylindrical block was sintered again at 1200 °C for 20 hours to obtain the EuCOB polycrystalline material.

2.2 Crystal growth

Single crystal growth was carried out by the Bridgman method. Compared with the Czochralski method, the Bridgman method has a simpler growth process, lower cost, and is more suitable for growing high-quality crystals. The crucible was a platinum crucible with a diameter of 25 mm and a length of 390 mm, and the seed crystal was placed at the bottom. The crystallographic *b*-direction SmCOB crystal with a diameter of 7 mm and a length of 35 mm was used as a seed crystal because the melting point of SmCOB is close to that of EuCOB (1480 °C). The furnace temperature was controlled at 1580 °C. The decrease rate of the crucible for single crystal growth is 0.333 mm h^{-1}. After crystal growth, the temperature was reduced to room temperature at a cooling rate of 25 °C h^{-1}. The platinum crucible was peeled off to obtain the EuCOB single crystal.

2.3 Characterization techniques

The phase structure of the EuCOB crystal was analyzed with a Bruker D8 diffractometer with Cu Kα radiation (λ = 1.54056 Å) at a high voltage of 40 kV and a current of 40 mA. The scanning step was set to 0.02°, and the scanning range was set from 10° to 70°. The (201) and (060) planes were measured by using an X-ray directional instrument (YX-2H8A embedded X-ray crystal orientator) to determine the crystallographic *a*-axis, *b*-axis and *c*-axis of the EuCOB crystal. According to the IEEE piezoelectric standard, different sizes of crystal samples were prepared, including square plates and rectangular plates. The length : width : thickness of the square plates is 10 : 10 : 1, and the length : width : thickness of the rectangular plates is (10–20) : (2–3) : (0.8–1). In addition, the surface of the crystal sample was coated with platinum by the spraying method for subsequent tests. The rocking curve of the (060) plane of EuCOB crystals was measured using a two-dimensional detector X-ray diffractometer (D8 DISCOVER, BRUKER, Germany). The thermal conductivity, thermal diffusivity and specific heat of the *X*, *Y* and *Z* planes of the EuCOB crystal were measured with a laser thermal conductivity meter (LFA457, NETZSCH, Germany). The sample size for the thermal performance measurement is 10 × 10 × 1 mm^3. The resonance and anti-resonance frequencies of the length extension vibration and shear vibration of the samples were measured using a LCR tester (IM-3536). The capacitance and dielectric loss of the samples were measured with a LCR tester (IM-3536). The electrical resistivity of the *X*, *Y* and *Z* planes of the EuCOB crystal was measured and calculated by using a super megohmmeter (HIOKI SM7110).

3. Results and discussion

3.1 Crystal quality

Fig. 1a shows the photograph of the as-grown EuCOB crystal. The whole crystal is pale pink and transparent. No inclusion and cracking can be seen in the crystal. The pink polycrystalline area near the tail of the EuCOB crystal is due to the incomplete growth, while the gray-black segregation

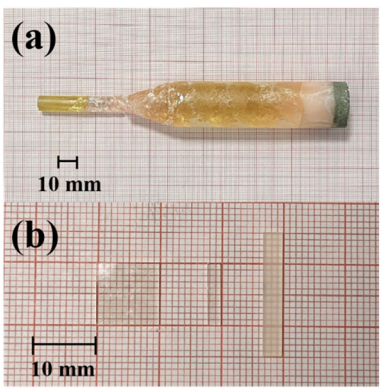

Fig. 1 Photographs of (a) the as-grown EuCOB crystal and (b) the piezoelectric test samples.

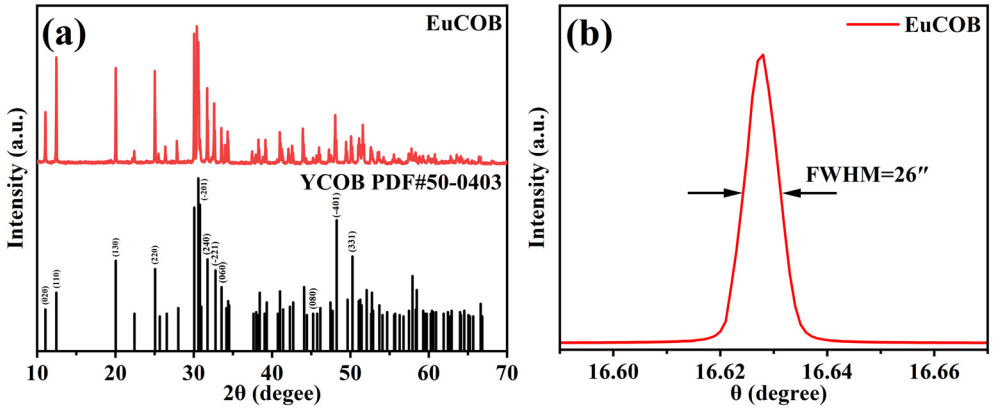

Fig. 2 (a) Powder XRD patterns of the EuCOB crystal and the (b) rocking curve of the (060) plane of the EuCOB crystal.

layer at the tail is due to impurity removal from the molten EuCOB. The phase structure of the pink polycrystalline was tested and analyzed by XRD, which was consistent with that of the EuCOB crystal. Fig. 1b shows the piezoelectric test samples obtained after crystal orientation, cutting and polishing, and their sizes are 10 × 10 × 1 mm^3, 10 × 2 × 1 mm^3 and 20 × 3 × 1 mm^3, respectively.

3.2 Crystal structure

The EuCOB transparent single crystal was ground into powders for XRD measurement, as shown in Fig. 2a. The diffraction peak of the EuCOB crystal is strong, indicating the high crystallinity. Compared with the YCOB standard card (PDF#50-0403), the peak position is basically the same, indicating that EuCOB has the same lattice structure as YCOB, belonging to the monoclinic system, m point group and C_m space group. In order to further characterize the crystal quality of the crystal, the rocking curve of the (060) plane of the EuCOB crystal was plotted, as shown in Fig. 2b. The diffraction peak is well symmetrical, and the half-peak width (FWHM) of the rocking curve is 26″. The result is close to the previous report, suggesting the excellent crystal quality.[38] The cell parameters of EuCOB and YCOB crystals are shown in Table 1. The results show that the lattice parameters of the EuCOB crystal are similar to those of EuCOB and YCOB crystals reported previously.

3.3 Thermal properties

Thermal performance plays an important role in high-temperature piezoelectric applications, which is related to the stability of working in a high-temperature environment. Therefore, the thermal conductivity, thermal diffusivity and specific heat of the EuCOB crystal were measured on the *X*, *Y* and *Z* planes, as shown in Fig. 3. Fig. 3a shows the thermal conductivity of the EuCOB crystal from room temperature to 800 °C, which decreases first and then increases with the increase of temperature. At 800 °C, the thermal conductivity of the *Z* plane of the EuCOB crystal is the largest, reaching 2.605 W m^{-1} K^{-1}, while the thermal conductivities of the *X* and *Y* planes are 2.433 W m^{-1} K^{-1} and 2.556 W m^{-1} K^{-1}, respectively. At room temperature, the thermal conductivities of the *X*, *Y* and *Z* planes of the EuCOB crystal are 1.798 W m^{-1} K^{-1}, 1.9 W m^{-1} K^{-1} and 2.458 W m^{-1} K^{-1}, respectively, which are similar to those of YCOB.[40] Fig. 3b shows the thermal diffusivity of the EuCOB crystal from room temperature to 800 °C, which decreases first and then increases with the increase of temperature. The thermal diffusivities of the *X*, *Y* and *Z* planes were 0.815 mm^2 s^{-1}, 0.789 mm^2 s^{-1}, and 1.054 mm^2 s^{-1} at room temperature, respectively, while changing to 0.589 mm^2 s^{-1}, 0.595 mm^2 s^{-1}, and 0.661 mm^2 s^{-1} at 800 °C, respectively. At the same temperature, the thermal conductivity and thermal diffusivity of the EuCOB crystal in different directions are different, which is related to the crystal anisotropy.[41,42]

Fig. 3c shows the specific heat of the EuCOB crystal from room temperature to 800 °C, which increases with the increase of temperature. From room temperature to 800 °C, the specific heat of the EuCOB crystal on the *X*, *Y* and *Z* planes gradually increases from 0.597 J g^{-1} K^{-1}, 0.652 J g^{-1} K^{-1}, and 0.632 J g^{-1} K^{-1} to 1.119 J g^{-1} K^{-1}, 1.163 J g^{-1} K^{-1}, and 1.068 J g^{-1} K^{-1}, respectively. The comparison of the EuCOB crystal with other high-temperature piezoelectric crystals is shown in Table 2. It can be seen that the thermal conductivity and thermal diffusivity of the EuCOB crystal are higher than those of the

Table 1 Lattice parameters of EuCOB and YCOB crystals

	a/Å	*b*/Å	*c*/Å	*α*/°	*β*/°	*γ*/°	Volume/Å^3	Ref.
EuCOB	8.0985	16.0332	3.5640	90.00	101.28	90.00	453.84000	This work
EuCOB	8.0966	16.0309	3.5670	90.00	101.29	90.00	454.02702	38
YCOB	8.0737	16.0088	3.5283	90.00	101.17	90.00	448.72000	39

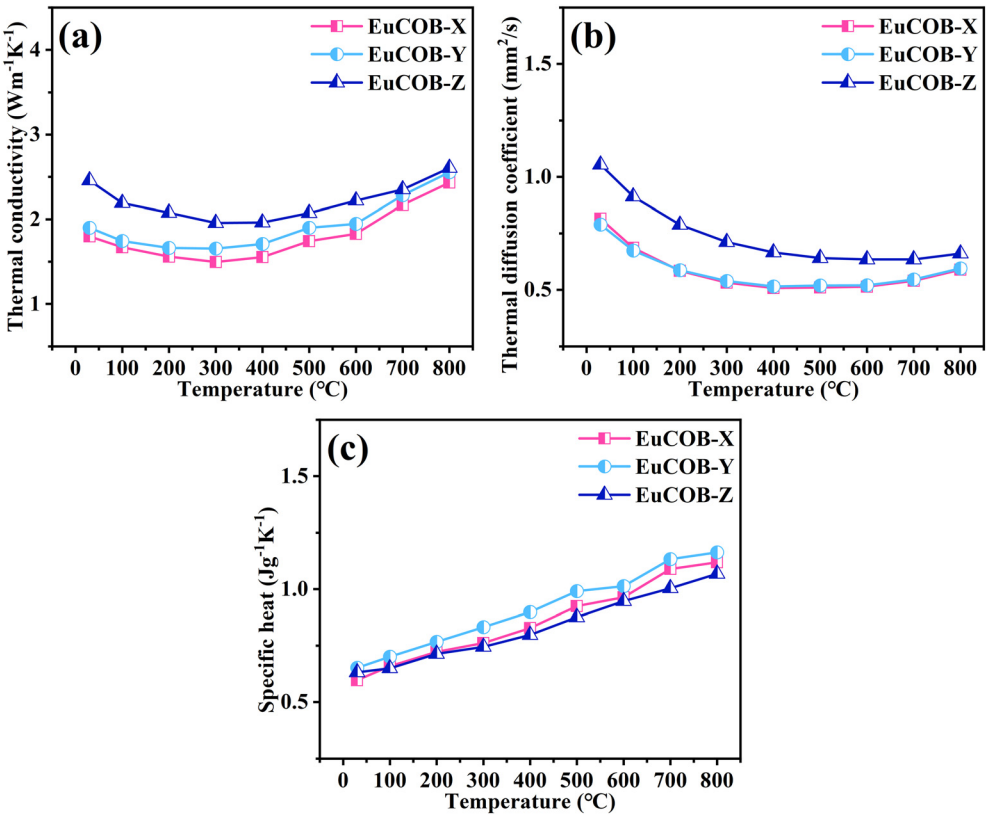

Fig. 3 (a) Thermal conductivity, (b) thermal diffusion and (c) specific heat of the EuCOB crystal as a function of temperature.

Table 2 Thermal properties of high-temperature piezoelectric crystals

Crystal	Thermal conductivity (W m^{-1} K^{-1})	Thermal diffusivity (mm^2 s^{-1})	Specific heat (J g^{-1} K^{-1})	Ref.
EuCOB	1.789–2.458 (298 K)	0.789–1.054 (298 K)	0.597–0.652 (298 K)	This work
YCOB	1.72–2.17 (373 K)	0.90 (293 K)	0.73 (373 K)	40, 43
CTGS	1.818–2.361 (300 K)	0.699–0.931 (300 K)	0.553–0.566 (300 K)	44

other two crystals. Higher thermal conductivity and thermal diffusivity can make the temperature to be uniformly distributed and prevent local overheating. The specific heat of the EuCOB crystal is higher than that of the CTGS crystal and smaller than that of the YCOB crystal. The greater the specific heat, the smaller the temperature change when absorbing the same heat. Meanwhile, the small thermal anisotropy of the EuCOB crystal ensures its thermal stability in high-temperature piezoelectric applications.

3.4 Dielectric, piezoelectric and elastic constant characterization

The dielectric constants ε_{11}, ε_{22} and ε_{33} of the EuCOB crystal can be determined by measuring the capacitance of the X, Y and Z square plates (10 × 10 × 1 mm^3) and calculating using eqn (1). The electromechanical coupling coefficient, elastic coefficient and piezoelectric coefficient of the EuCOB crystal can be obtained by the resonance–antiresonance method.[25] Among them, the electromechanical coupling coefficients k_{12} and k_{13}, elastic coefficients s_{22} and s_{33} and piezoelectric coefficients d_{12} and d_{13} can be derived from eqns (2)–(4) by measuring the resonance and antiresonance frequency of the transverse effect length-extensional vibration. The electromechanical coupling coefficients k_{24} and k_{26}, elastic coefficients s_{44} and s_{66} and piezoelectric coefficients d_{24} and d_{26} can be derived from eqns (4)–(6) by measuring the resonance and anti-resonance frequency of the longitudinal effect face-shear vibration.

$$\varepsilon^{T}_{11,22,33}/\varepsilon_0 = \frac{C_{11,22,33}\cdot t}{A\cdot\varepsilon_0} \quad (1)$$

$$\frac{k^2}{1-k^2} = \frac{\pi}{2}\frac{f_a}{f_r}\cot\left(\frac{\pi}{2}\frac{f_r}{f_a}\right) \quad (2)$$

$$s^E = \frac{1}{4\rho l^2 f_r^2} \quad (3)$$

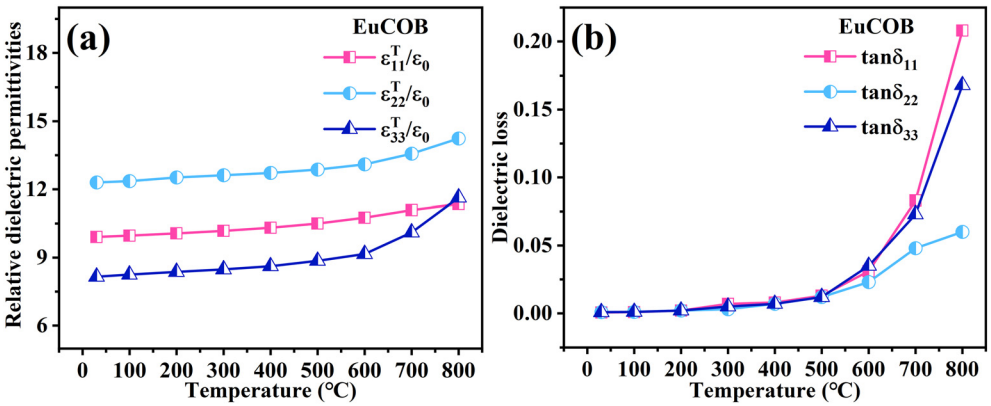

Fig. 4 (a) The relative dielectric permittivity and (b) dielectric loss of the EuCOB crystal as a function of temperature.

$$d = k(\varepsilon s)^{1/2} \quad (4)$$

$$k^2 = \frac{\pi}{2}\frac{f_r}{f_a}\tan\left(\frac{\pi}{2}\frac{f_a - f_r}{f_a}\right) \quad (5)$$

$$s^E = \frac{1}{4w^2 f_a{}^2 \rho(1-k^2)} \quad (6)$$

where C is the capacitance, t is the thickness, A is the square plate area, ε_0 is the vacuum dielectric constant, f_r is the resonant frequency, f_a is the anti-resonant frequency, ρ is the density, l is the length, and w is the width.[25]

Fig. 4 shows the variation of the relative dielectric permittivity and dielectric loss of the EuCOB crystal from room temperature to 800 °C at 100 kHz. The relative dielectric permittivities $\varepsilon_{11}^T/\varepsilon_0$, $\varepsilon_{22}^T/\varepsilon_0$ and $\varepsilon_{33}^T/\varepsilon_0$ increase with the increase of temperature, from 9.91, 12.3 and 8.16 at room temperature to 11.36, 14.24 and 11.64 at 800 °C, respectively. The $\varepsilon_{33}^T/\varepsilon_0$ has the highest variation rate of 42.6%, while the variation rates of $\varepsilon_{11}^T/\varepsilon_0$ and $\varepsilon_{22}^T/\varepsilon_0$ are 14.6% and 15.8%, respectively. The dielectric losses $\tan\delta_{11}$, $\tan\delta_{22}$ and $\tan\delta_{33}$ of the EuCOB crystal are less than 0.1% at room temperature, indicating a high crystal quality and few defects. As shown in Fig. 4b, the dielectric loss increases with increasing temperature, and increases significantly after 500 °C, which is related to the excitation of a large number of electrons at high temperature. Due to heat promotion, a large number of electrons are excited at higher temperatures, which reduces the electrical resistivity and significantly increases the dielectric loss.[45] At 800 °C, the dielectric loss $\tan\delta_{22}$ is 6%, which is significantly lower than the 20.8% of $\tan\delta_{11}$ and the 16.8% of $\tan\delta_{33}$. The relatively low dielectric loss of the EuCOB crystal can improve its efficiency and stability in high-temperature piezoelectric applications.

The resonance frequency and anti-resonance frequency of different EuCOB samples were measured, including the d_{12} and d_{13} of the transverse effect length-extensional vibration and the d_{24} and d_{26} of the longitudinal effect face-shear vibration. Fig. 5a shows the variation of the impedance modulus of the longitudinal effect face-shear vibration mode (d_{26}) of the EuCOB crystal as a function of temperature. From room temperature to 800 °C, the resonance peaks are observed in the frequency range of 540 to 590 kHz. The resonance peak moves to a lower frequency as the temperature increases. The variation of the resonance frequency of different EuCOB crystal cuts with increasing temperature is shown in Fig. 5b. In the temperature range from room temperature to 800 °C, the resonant frequency

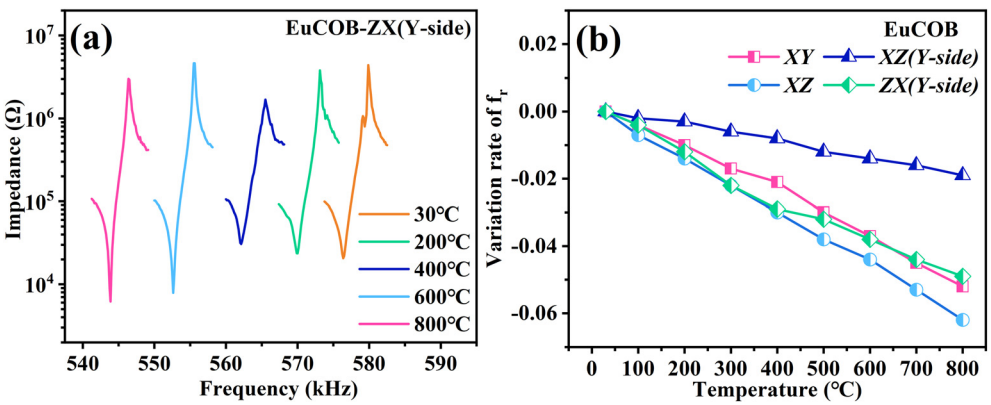

Fig. 5 (a) The impedance modulus of the longitudinal effect face-shear vibration mode (d_{26}) and (b) the variation of the resonance frequency of the EuCOB crystal as a function of temperature.

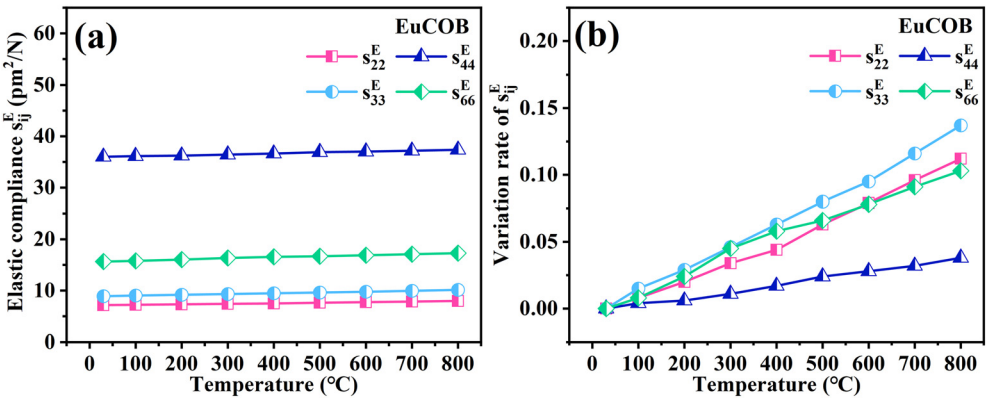

Fig. 6 (a) The elastic compliance and (b) variation rate of the s_{ij}^E of the EuCOB crystal as a function of temperature.

of each crystal cut decreases with the increase of temperature, showing a linear relationship. The change of the resonant frequency of the *XZ* crystal cut is the largest.

The corresponding elastic compliances s_{22}, s_{33}, s_{44} and s_{66} were calculated according to eqns (3) and (6), and the dependence with temperature is shown in Fig. 6. The elastic compliances s_{22}, s_{33}, s_{44} and s_{66} increase with the increase of temperature, with the variation rates of 11.2%, 13.7%, 3.8% and 10.3%, respectively. Based on the measured resonant and anti-resonant frequencies, according to the calculation equation it can be concluded that the increasing of the elastic coefficient is related to the fact that the resonant and anti-resonant frequency transferred to the lower frequency as the temperature increases.

The electromechanical coupling coefficient k_{ij} and piezoelectric coefficient d_{ij} of the EuCOB crystal are calculated using eqns (2), (4) and (5), based on the determined resonant frequency and anti-resonant frequency, elastic coefficient and

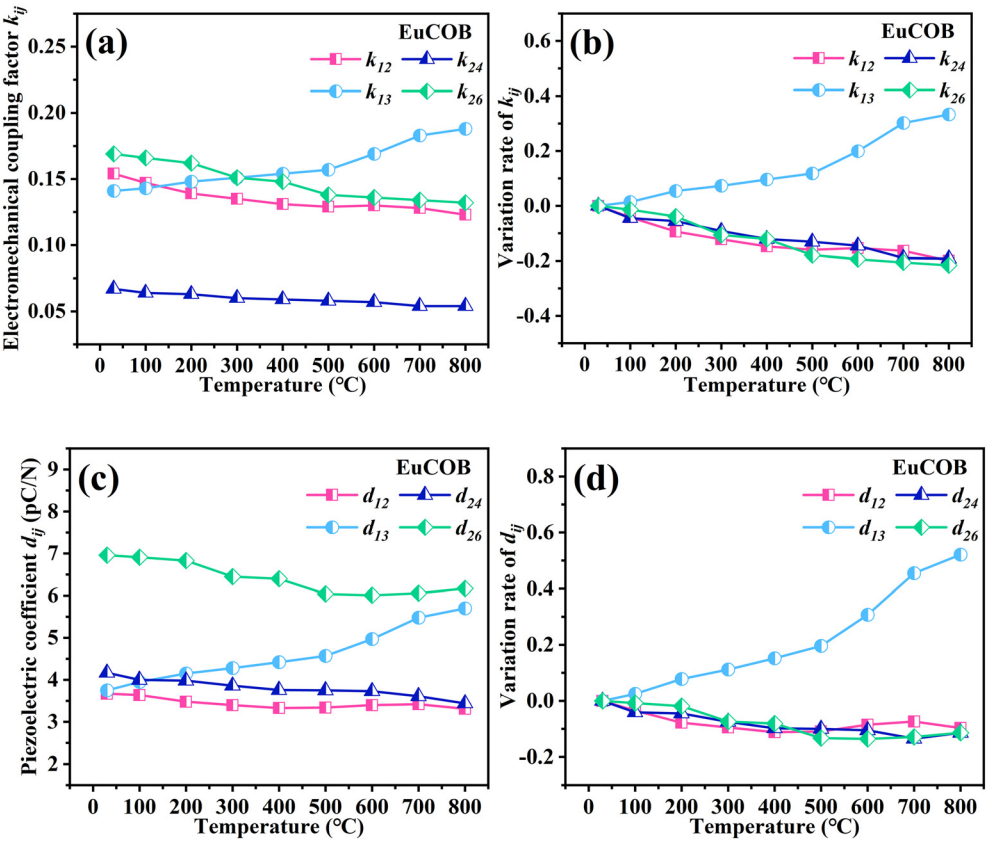

Fig. 7 (a) The electromechanical coupling coefficient, (b) variation rate of k_{ij}, (c) piezoelectric coefficient and (d) variation rate of the d_{ij} of the EuCOB crystal as a function of temperature.

dielectric coefficient. Fig. 7 shows the variation of the electromechanical coupling coefficient k_{ij} and piezoelectric coefficient d_{ij} with increasing temperature. Different electromechanical coupling coefficients exhibited different trends, where the k_{13} increases with increasing temperature, while the k_{12}, k_{24} and k_{26} show the decreasing trend over the measured temperature range. The variation rate of k_{13} is calculated to be 33.3% from room temperature to 800 °C, which is the largest, while the variation rates of k_{12}, k_{24} and k_{26} are 20.0%, 19.2% and −21.6%, respectively. It can be observed that the trend of the electromechanical coupling coefficient k_{ij} and piezoelectric coefficient d_{ij} with increasing temperature is similar. The d_{13} increases from 3.96 pC N^{-1} at room temperature to 6.02 pC N^{-1} at 800 °C, showing a large variation rate of 52.1%, while the d_{12} and d_{24} decrease slightly with the increase of temperature, showing small variation rates of 9.7% and 11.4%, respectively. For the shear piezoelectric coefficient d_{26} of the EuCOB crystal, it decreases slightly with the increase of temperature, from 7.02 pC N^{-1} at room temperature to 6.22 pC N^{-1} at 800 °C, with a variation rate of only 11.4%, showing the advantage of high-temperature piezoelectric application.

3.5 Electrical resistivity

Electrical resistivity is an important parameter that determines whether the piezoelectric crystal can be applied at high temperature. The electrical resistivities of the EuCOB crystal along the *X*, *Y* and *Z* directions were measured from 400 °C to 800 °C at a voltage of 100 V, as shown in Fig. 8. It can be found that the electrical resistivity of the EuCOB crystal follows the Arrhenius formula from 400 °C to 800 °C. The activation energy E_a was calculated using the Arrhenius formula:[44]

$$\rho = \rho_0 \exp\left(\frac{E_a}{k_B T}\right) \quad (7)$$

where ρ is the electrical resistivity, ρ_0 is the ultimate resistivity at an infinite temperature, E_a is the activation energy, K_B is the Boltzmann constant, and T is the absolute temperature. The calculated activation energies E_a of the EuCOB crystal along the *X*, *Y* and *Z* directions are 1.02 eV, 1.13 eV and 1.06 eV, which are slightly lower than the activation energy E_a of the CTGS crystal (1.20 eV).[46] The electrical resistivity of the EuCOB crystal decreases with the increase of temperature, and the electrical resistivities of the three directions are different, which reflects the anisotropy of the electrical resistivity of the EuCOB crystal. The test results show that the electrical resistivity of the EuCOB crystal measured in the *X* direction is higher than that in the *Y* and *Z* directions. The electrical resistivity in the *X* direction is 5.8×10^7 Ω cm at 800 °C, which is one order of magnitude higher than that of CTGS (10^6–10^7 Ω cm at 800 °C), showing the potential for high-temperature piezoelectric applications.[46]

The electrical resistivity is affected by microscopic crystal defects and band gaps.[45] At relatively low temperatures (generally <600 °C), the conductivity of the EuCOB crystal is dominated by the migration of oxygen vacancies, which are crystal defects (hole–electron pairs) and introduce extra energy levels in the band gap, as shown in Fig. 9a and b. As the temperature increases, the concentration of vacancies increases, leading to a decrease in the electrical resistivity and an increase in the conductivity of the EuCOB crystal. When the temperature reaches a certain value (generally >600 °C), the electrons will jump from the valence band to the conduction band and play a dominant role, as shown in Fig. 9c, which explains the significant increase in the dielectric loss, as shown in Fig. 4b.[45] Therefore, at relatively

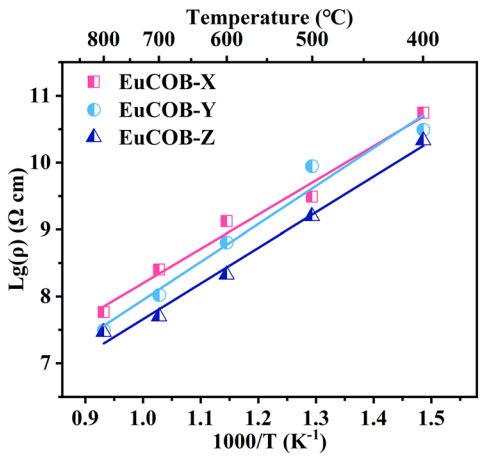

Fig. 8 Electrical resistivity of the EuCOB crystal as a function of temperature.

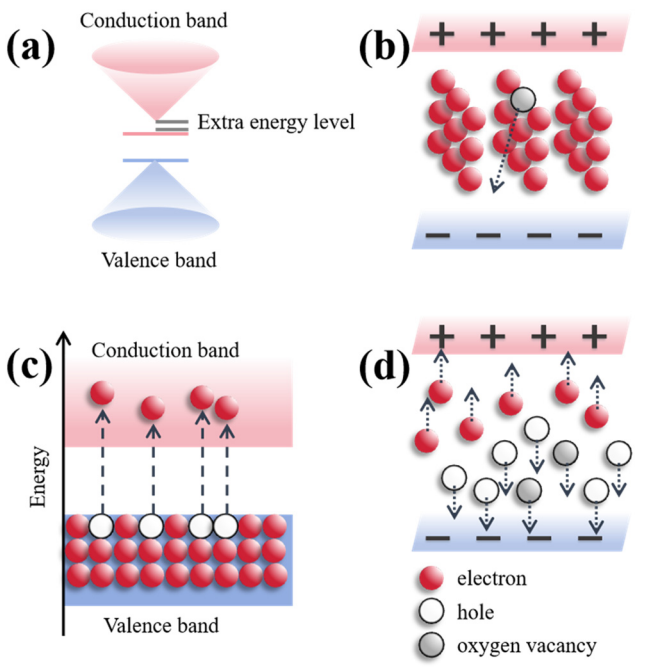

Fig. 9 The conduction mechanism model of the EuCOB crystal: (a) the defect energy level between the conduction band and valence band, (b) oxygen vacancy migration, (c) electronic migration between the conduction band and valence band, and (d) electron–hole and oxygen vacancy migration.

low temperatures, the electrical resistivity of the EuCOB crystal is mainly affected by oxygen vacancy defects (hole–electron pairs), whereas at relatively high temperatures, both the oxygen vacancies and the band gap of the EuCOB crystal affect the electrical resistivity, as shown in Fig. 9d.

4. Conclusions

A EuCOB single crystal with a diameter of 25 mm was successfully grown by the Bridgman method. The measured half peak width of the rocking curve is 26″ for the (060) plane of the EuCOB crystal, indicating good crystal quality. The thermal conductivity, thermal diffusivity and specific heat of the EuCOB crystal along the *Y* direction are 1.9 W m^{-1} K^{-1}, 0.789 mm^2 s^{-1} and 0.652 J g^{-1} K^{-1} at room temperature, and 2.546 W m^{-1} K^{-1}, 0.593 mm^2 s^{-1} and 1.161 J g^{-1} K^{-1} at 800 °C, respectively. In the range of room temperature to 800 °C, the dielectric coefficient, elastic coefficient and piezoelectric coefficient of the EuCOB crystal have good temperature stability. In particular, the shear piezoelectric coefficient d_{26} of the EuCOB crystal is 7.01 pC N^{-1} at room temperature, and 6.22 pC N^{-1} at 800 °C, maintaining high piezoelectric properties at high temperature. The electrical resistivities of the EuCOB crystal along the *X*, *Y* and *Z* directions at 800 °C are 5.8×10^7 Ω cm, 3.1×10^7 Ω cm and 2.9×10^7 Ω cm, respectively, which are one order of magnitude higher than those of the CTGS crystal, reflecting the potential of high-temperature piezoelectric applications. Finally, the conduction mechanism model of the EuCOB crystal is presented, which explains the relationship between the electrical resistivity, crystal defects and band gap of the EuCOB crystal with temperature.

Data availability

The authors state that this work is original. All authors have agreed to the manuscript submission and confirm that the work has not been submitted simultaneously to another journal for consideration. In addition, all authors declare no conflicts of interest.

Conflicts of interest

The authors declare that they have no known competing financial interests or personal relationships that could have appeared to influence the work reported in this paper.

Acknowledgements

This work is supported by the National Natural Science Foundation of China (No. 51832009) and the Yongjiang Talent Project (2021A-048-C). This work is also sponsored by the K. C. Wong Magna Foundation in Ningbo University.

References

1 Y. Meng, G. Chen and M. Huang, *Nanomaterials*, 2022, **12**, 1171.
2 M. J. Schulz, M. J. Sundaresan, J. McMichael, D. Clayton, R. Sadler and B. Nagel, *J. Intell. Mater. Syst. Struct.*, 2016, **14**, 693–705.
3 S. Zhang, F. Yu and D. J. Green, *J. Am. Ceram. Soc.*, 2011, **94**, 3153–3170.
4 F. Yu, S. Zhang, X. Zhao, S. Guo, X. Duan, D. Yuan and T. R. Shrout, *J. Phys. D: Appl. Phys.*, 2011, **44**, 135405.
5 X. Fu, E. G. Víllora, Y. Matsushita, Y. Kitanaka, Y. Noguchi, M. Miyayama, K. Shimamura and N. Ohashi, *J. Alloys Compd.*, 2021, **851**, 156860.
6 F. Yu, S. Hou, X. Zhao and S. Zhang, *IEEE Trans. Ultrason. Ferroelectr. Freq. Control*, 2014, **61**, 1344–1356.
7 S. Zhang, E. Frantz, R. Xia, W. Everson, J. Randi, D. W. Snyder and T. R. Shrout, *J. Appl. Phys.*, 2008, **104**, 084103.
8 S. Zhang, F. Li, F. Yu, X. Jiang, H.-Y. Lee, J. Luo and T. R. Shrout, *J. Korean Ceram. Soc.*, 2018, **55**, 419–439.
9 H. Zu, H. Wu and Q.-M. Wang, *IEEE Trans. Ultrason. Ferroelectr. Freq. Control*, 2016, **63**, 486–505.
10 J. Haines, O. Cambon, D. A. Keen, M. G. Tucker and M. T. Dove, *Appl. Phys. Lett.*, 2002, **81**, 2968–2970.
11 S. Bouchy, R. J. Zednik and P. Bélanger, *Materials*, 2022, **15**, 4716.
12 D. Damjanovic, *Curr. Opin. Solid State Mater. Sci.*, 1998, **3**, 469–473.
13 L. Bai, D. Liu, X. Zhao, F. Yu and Y. Li, *ACS Appl. Mater. Interfaces*, 2023, **15**, 3152–3162.
14 A. K. Nagmani and B. Behera, *IEEE Trans. Ultrason. Ferroelectr. Freq. Control*, 2022, **69**, 918–931.
15 F. Holger, *Meas. Sci. Technol.*, 2011, **22**, 012002.
16 S. Zhang, Y. Zheng, H. Kong, J. Xin, E. Frantz and T. R. Shrout, *J. Appl. Phys.*, 2009, **105**, 114107–114113.
17 S. Zhang, A. Yoshikawa, K. Kamada, E. Frantz, R. Xia, D. W. Snyder, T. Fukuda and T. R. Shrout, *Solid State Commun.*, 2008, **148**, 213–216.
18 J. Bohm, R. B. Heimann, M. Hengst, R. Roewer and J. Schindler, *J. Cryst. Growth*, 1999, **204**, 128–136.
19 G. Yao, F. Chen, F. Yu and X. Zhao, *J. Rare Earths*, 2022, **40**, 1772–1777.
20 S. Tian, C. Jiang, F. Chen, F. Yu, X. Cheng, S. Zhang, Z. Wang and X. Zhao, *Cryst. Growth Des.*, 2020, **20**, 2651–2659.
21 X. Lu, L. Li, S. Tian, Y. Li, F. Yu, X. Cheng and X. Zhao, *J. Mater. Chem. C*, 2020, **8**, 10109–10120.
22 K. Kim, S. Zhang, G. Salazar and X. Jiang, *Sens. Actuators, A*, 2012, **178**, 40–48.
23 K. Kim, S. Zhang, W. Huang, F. Yu and X. Jiang, *J. Appl. Phys.*, 2011, **109**, 126103–126103.
24 F. Yu, S. Zhang, X. Zhao, D. Yuan, C.-M. Wang and T. R. Shrout, *Cryst. Growth Des.*, 2010, **10**, 1871–1877.
25 T. Karaki, M. Adachi and Y. Kuniyoshi, *J. Electroceram.*, 2007, **21**, 823–826.
26 H. Shimizu, K. Kodama, H. Takeda, T. Nishida, T. Shikida, S. Okamura and T. Shiosaki, *Jpn. J. Appl. Phys.*, 2004, **43**, 6716–6720.
27 M. Münchhalfen, J. Schreuer, C. Reuther, E. Mehner and H. Stöcker, *J. Appl. Phys.*, 2021, **130**, 095102.

28 H. Zu, Y. Zheng and Q.-M. Wang, *J. Appl. Phys.*, 2019, **126**, 045104.
29 F. Yu, X. Duan, S. Zhang, Q. Lu and X. Zhao, *Crystals*, 2014, **4**, 241–261.
30 H. Shimizu, T. Nishida, H. Takeda and T. Shiosaki, *J. Cryst. Growth*, 2009, **311**, 916–920.
31 C. Pawlaczyk, E. Markiewicz, A. Kłos, W. Hofman and A. Pajączkowska, *Phys. Status Solidi A*, 2006, **203**, 2103–2118.
32 K. Xiong, X. Tu, Z. Man, S. Wang, Y. Zheng, T. Karaki and E. Shi, *CrystEngComm*, 2022, **24**, 4294–4300.
33 K. Xiong, S. Wang, X. Tu, Y. Zheng, T. Karaki and E. Shi, *J. Cryst. Growth*, 2020, **535**, 125525.
34 S. Hou, F. Yu, Y. Liu, S. Zhang, Q. Lu, S. Wang and X. Zhao, *CrystEngComm*, 2015, **17**, 553–560.
35 F. Yu, S. Hou, S. Zhang, Q. Lu and X. Zhao, *Phys. Status Solidi A*, 2013, **211**, 574–579.
36 S. Zhang, F. Yu, R. Xia, Y. Fei, E. Frantz, X. Zhao, D. Yuan, B. H. T. Chai, D. Snyder and T. R. Shrout, *J. Cryst. Growth*, 2011, **318**, 884–889.
37 F. Yu, S. Zhang, X. Zhao, D. Yuan, Q. Wang and T. R. Shrout, *Phys. Status Solidi RRL*, 2010, **4**, 103–105.
38 C. Yang, T. Liang, Z. Sun, L. Jiang, L. Wang, H. Qian and Y. Zheng, *Cryst. Growth Des.*, 2024, **24**, 7561–7569.
39 R. Möckel, C. Reuther and J. Götze, *J. Cryst. Growth*, 2013, **371**, 70–76.
40 F. Yu, S. Zhang, X. Cheng, X. Duan, T. Ma and X. Zhao, *CrystEngComm*, 2013, **15**, 5226–5231.
41 T. Liang, L. Jiang, Z. Sun, C. Yang, H. Qian, T. Zhao, L. Ai and Y. Zheng, *J. Cryst. Growth*, 2024, **634**, 127686.
42 T.-H. Liu and C.-C. Chang, *Nanoscale*, 2015, **7**, 10648–10654.
43 J. Luo, S. J. Fan, H. Q. Xie, K. C. Xiao, S. X. Qian, Z. W. Zhong, G. X. Qiang, R. Y. Sun and J. Y. Xu, *Cryst. Res. Technol.*, 2001, **36**, 1215–1221.
44 L. Ai, Z. Sun, L. Jiang, J. Pan, Y. Zheng and S. Pan, *CrystEngComm*, 2024, **26**, 1550–1555.
45 S. Tian, L. Li, X. Lu, F. Yu, Y. Li, C. Jiang, X. Duan, Z. Wang, S. Zhang and X. Zhao, *Acta Mater.*, 2020, **183**, 165–171.
46 K. Xiong, S. Wang, X. Tu, Z. Man, Y. Zheng, T. Karaki and E. Shi, *CrystEngComm*, 2021, **23**, 5362–5366.

